

Article

Efficient Hydrogen Production from the Aqueous-Phase Reforming of Biomass-Derived Oxygenated Hydrocarbons over an Ultrafine Pt Nanocatalyst

Ze Xiao ^{1,†}, Xi Lin ^{1,†}, Wenhua Feng ¹, Binyi Chen ¹, Qingwei Meng ^{1,*} and Tiejun Wang ^{1,2,*}

¹ School of Chemical Engineering and Light Industry, Guangdong University of Technology, Guangzhou 510006, China

² Graduate School, Guangdong University of Technology, Guangzhou 510006, China

* Correspondence: qwmeng@gdut.edu.cn (Q.M.); tjwang@gdut.edu.cn (T.W.)

† These authors contributed equally to this work.

Abstract: Hydrogen from biomass, as a promising alternative fuel, is becoming considerably attractive due to its high energy density and clean emissions. The aqueous phase reforming (APR) of biomass-derived oxygenated hydrocarbons and water is a renewable and efficient pathway for hydrogen production and shows great potential. However, the key to the application of this technique is to develop catalysts with high hydrogen productivity. In this work, we first synthesized polyaniline-platinum (PANI-Pt) organo-metallic hybrid precursors and then obtained a high-loaded (~32 wt.% Pt) and highly dispersed (~3 nm Pt particles) Pt@NC-400 catalyst after pyrolysis at 400 °C, and the nanoparticles were embedded in a nitrogen-doped carbon (NC) support. The Pt@NC-400 catalyst showed an almost three times higher hydrogen production rate (1013.4 $\mu\text{mol}_{\text{H}_2}/\text{g}_{\text{cat.}}/\text{s}$) than the commercial 20% Pt/C catalyst (357.3 $\mu\text{mol}_{\text{H}_2}/\text{g}_{\text{cat.}}/\text{s}$) for catalyzing methanol-water reforming at 210 °C. The hydrogen production rate of 1,2-propanediol APR even reached 1766.5 $\mu\text{mol}_{\text{H}_2}/\text{g}_{\text{cat.}}/\text{s}$ over the Pt@NC-400 catalyst at 210 °C. In addition, Pt@NC-400 also exhibited better hydrothermal stability than 20% Pt/C. A series of characterizations, including ICP, XRD, TEM, SEM, XPS, N₂ physisorption, and CO chemisorption, were conducted to explore the physiochemical properties of these catalysts and found that Pt@NC-400, although with higher loading than 20% Pt/C (~23 wt.% Pt, ~4.5 nm Pt particle), possessed a smaller particle size, a more uniform particle distribution, a better pore structure, and more Pt metal active sites. This study provides a strategy for preparing high-loaded and highly dispersed nanoparticle catalysts with high hydrogen productivity and sheds light on the design of stable and efficient APR catalysts.

Keywords: oxygenated hydrocarbons; Pt@NC catalysts; aqueous phase reforming; hydrogen production



Citation: Xiao, Z.; Lin, X.; Feng, W.; Chen, B.; Meng, Q.; Wang, T. Efficient Hydrogen Production from the Aqueous-Phase Reforming of Biomass-Derived Oxygenated Hydrocarbons over an Ultrafine Pt Nanocatalyst. *Catalysts* **2023**, *13*, 1428. <https://doi.org/10.3390/catal13111428>

Academic Editor: Leonarda Liotta

Received: 14 October 2023

Revised: 7 November 2023

Accepted: 10 November 2023

Published: 12 November 2023



Copyright: © 2023 by the authors. Licensee MDPI, Basel, Switzerland. This article is an open access article distributed under the terms and conditions of the Creative Commons Attribution (CC BY) license (<https://creativecommons.org/licenses/by/4.0/>).

1. Introduction

Resolving the conflicts between economic growth and environmental protection, as well as upgrading the global energy system for sustainable development, is becoming a major concern and policy objective. As a clean and renewable energy source, biomass-derived hydrogen is considered to be one of the most promising alternatives to fossil energy sources in the future [1–5]. Nowadays, hydrogen is widely used in various fields, especially in polymer electrolyte membrane fuel cells (PEMFCs). Due to their low operating temperature, high power density, and high energy conversion efficiency, PEMFCs driven by H₂ are an attractive and alternative power source [6–10]. Recent work exploring hydrogen sources for portable PEMFCs has focused on hydrogen production from the aqueous phase reforming of methanol (APRM), which allows for the direct integration of a compact hydrogen production device into the PEMFC with low-energy consumption and ease of implementation [7].

Compared with other traditional hydrogen production methods, such as methanol decomposition, partial oxidative reforming, and steam reforming, APR has many advantages, such as a low conversion temperature, low energy consumption, high hydrogen utilization, a high hydrogen production rate, etc. [11–15]. The latest reviews [16,17] point out that not only the type of active metal but also the choice of support and different preparation methods can have a great influence on the performance of APR catalysts, and they also call for the study of catalysts to take into account practical application scenarios, such as APR for biorefinery wastewater. The main challenge of APR for hydrogen production nowadays is still developing highly efficient catalysts. Meanwhile, an active metal catalyst with high metal loading and high metal dispersion could be an effective solution. According to previous research, platinum-based catalysts show high catalytic activity in the APR processes and have promising development prospects [6,7,18]. It has also been shown that conventionally supported metal catalysts usually require high temperatures and high loading to obtain a good reaction performance, whereas carbon-supported Pt particles seem to be more active than non-carbon-supported ones [19,20]. In addition, the size of the metal particles is also crucial for the catalyst to perform its function. For instance, catalysts with a Pt particle size in the range of 2–5 nm and a narrow and uniform distribution exhibit better activity and stability [21].

In addition, since the APR operating temperature is usually 200–250 °C and an unstable support, it could lead to the aggregation or leaching of the active metal; the choice of the support is critical for the stability of APR catalysts, which requires enough hydrothermal stability for candidate supports. For example, the Al₂O₃ support in the widely used Pt/Al₂O₃ catalyst is prone to hydrolysis under hydrothermal conditions, leading to catalyst deactivation [22,23]. By contrast, the carbonaceous material is a kind of hydrothermal, acid- and base-resistant support. Carbon-supported Pt/C catalysts have shown excellent performance in hydrothermal reactions, including APR processes [24,25]. However, Pt particles are usually not uniform in size and are basically loaded on the surface of the carbon support, especially those prepared by impregnation and precipitation methods. Thus, Pt particles also have the possibility of being agglomerated under harsh hydrothermal conditions because of the weak interaction between particles and support, ultimately leading to the degradation of catalytic activity [25,26]. Single-atom Pt-based catalysts, which increase their contact or interaction between the Pt and support, have also been proposed to improve the stability of catalysts and have indeed shown good performance in APR reactions [7,27,28]. However, the hydrogen productivity of single-atom catalysts is not satisfactory due to their low metal loading, and those catalysts are often difficult to prepare and also have the risk of solitary atom detachment or aggregation, thus making the catalyst deactivate. Therefore, the exploitation of a feasible preparation strategy for the carbon-based Pt catalyst with high Pt loading as well as superior Pt dispersion could be an ideal solution to improve both the hydrogen productivity and hydrothermal durability of the APR.

Previous studies have introduced a feasible method for the preparation of polyaniline polystyrene sulfonate platinum (PANI-PSS-Pt) composites via interfacial polymerization, by which uniform Pt nanoparticles down to 2 nm were obtained [29–31]. In this method, aniline, chloroplatinate ions, and polystyrene sulfonate were used as the monomer, oxidizing agent, and solvent medium, respectively. Then, while aniline was oxidized to polyaniline, chloroplatinate ions were simultaneously reduced to Pt nanoparticles, resulting in the formation of the PANI-Pt/PSS nanocomplex. The superiority of this method lies in the fact that the formed PANI polymer as a capping reagent with a nanosized fiber-like morphology and large specific surface area can adequately disperse the Pt nanoparticles. Additionally, the intimate contact between PANI and Pt nanoparticles can tightly anchor and control the nanoparticles, improving their stability. Therefore, the aggregation of Pt particles is effectively suppressed due to the strong interaction between PANI and Pt particles during the high-temperature pyrolysis of the PANI-Pt complex. This indicates that PANI contributes to restricting the migration of Pt particles and can be a promising carbon

support for heterogeneous catalysts [32,33]. This approach also has obvious drawbacks; for example, PSS is a toxic organic solvent that does not meet the principles of clean emissions in green chemistry. In addition, it has been shown that elemental sulfur may have a toxic effect on Pt catalysts.

In this study, we optimized the preparation method of the metal nanocomposite by removing the PSS solvent in order to avoid the inhibitory effect of element S on Pt active sites. In this scenario, the PANI-Pt precursor was prepared using a more facile approach, and a series of N-doped Pt@NC catalysts were obtained by employing different temperature pyrolysis treatments. The geometrical and electronic structures of the Pt@NC catalysts were analyzed using XRD, SEM, TEM, FTIR, and XPS techniques, and their catalytic performances for the APR reactions were tested at different temperatures and biomass-derived feedstocks. In comparison with the commercial 20% Pt/C catalyst, the Pt@NC-400 catalyst developed in this study showed remarkable superiority in terms of its microstructure, catalytic activity, and stability and can be an excellent candidate for industrial hydrogen production from APR.

2. Results and Discussion

2.1. Catalysts Properties

2.1.1. Crystalline Structure of the Pt@NC and 20% Pt/C Catalysts

The employed Pt@NC catalysts were synthesized, as shown in Figure 1. First, aniline and H_2PtCl_6 were dissolved in ethanol and water, respectively, and then the latter was added to the former. In this process, the strong oxidant PtCl_6^{2-} ion induces the oxidation and polymerization of aniline, along with its own reduction in Pt nanoparticles, resulting in a PANI-Pt complex, which can then be pyrolyzed at different temperatures to obtain the final Pt@NC catalysts. The pivotal step in this scheme is the formation of the hybrid PANI-Pt, which realizes the in situ confinement of Pt nanoparticles in the N-doped carbon material. The hydrothermal conditions of the APR can exhibit acidic properties, placing high requirements on the APR catalyst. As carbon material is highly acid resistant, the Pt@NC catalyst with the structure of carbon-encapsulated Pt nanoparticles was expected to exhibit good stability in the aqueous reforming process.

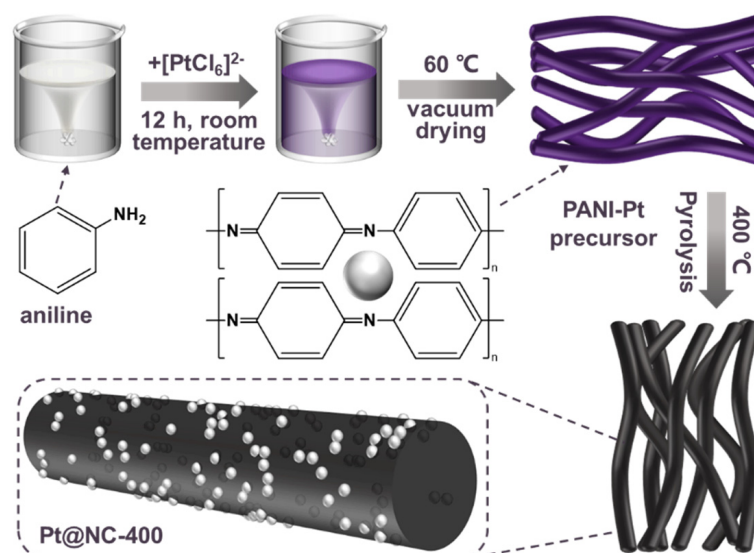


Figure 1. Schematic illustration for the synthesis procedure of the Pt@NC-400 catalyst.

Figure 2 shows the X-ray diffraction (XRD) pattern of the prepared Pt@NC catalyst. By comparing this with the standard card (JCPDS 04-0802), it was found that the diffraction peaks at 2θ of 39.7° , 46.2° , and 67.4° in Figure 2a,b correspond to the crystal plane reflections of Pt (111), (200), and (220), respectively, and all these crystalline phases belong to the

face-centered cubic crystal system of Fm3m (225) [18]. This demonstrates that Pt-based nanoparticle catalysts with similar crystalline phases can be successfully prepared from PANI-Pt precursors after pyrolysis at different temperatures.

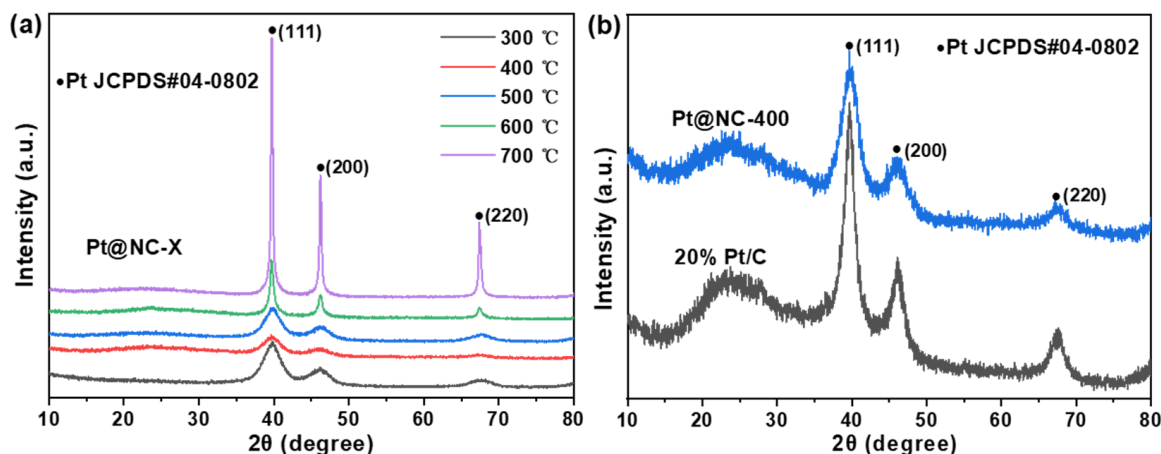


Figure 2. XRD diffraction patterns of (a) Pt@NC catalysts with different pyrolysis temperatures and (b) Pt@NC–400 and 20% Pt/C catalysts.

As can be seen from Figure 2a, the shapes of the XRD diffraction peaks of the Pt-based catalysts clearly vary at different pyrolysis temperatures. As the temperature increases, the diffraction peaks become sharper, which indicates that the particle size (3.4–24.8 nm, Table S1) of the Pt particles gradually increases. The half-peak width of the diffraction peak from the Pt@NC–300 is the widest, which indicates that its Pt particle size is the smallest. As shown in Figure 2b and Table S2, the observed Pt crystalline phases of the Pt@NC–400 and 20% Pt/C catalysts are the same, although the former has a higher Pt loading than the latter (32.2 wt.% and 22.9 wt.%, respectively), and the diffraction peaks of the latter are much sharper, suggesting a smaller particle size and a higher degree of particle dispersion of the Pt@NC–400.

2.1.2. Morphology and Structure of the Pt@NC Catalysts

The micro-structures of the Pt@NC catalysts at different calcination temperatures were investigated through the transmission electron microscope (TEM), and the TEM images are shown in Figure 3a–d. It can be clearly seen that the dispersion of metal nanoparticles became poorer with the increase in the pyrolysis temperature. Below 500 °C, the Pt particle size increases slightly with the rising pyrolysis temperature, whereas above 500 °C, the particle size increases rapidly, which could be due to the carbonization temperature becoming closer to the T_m of metal Pt (750 °C). The size statistics results from the inset show that the particle size increases from 3.5 nm to 15.4 nm, which is also in good agreement with the XRD results calculated using the Scherrer formula (Table S1). The TEM results of the 20% Pt/C catalyst showed that although the average Pt particle size was not too large, only about 4.5 nm, its particle distribution was highly nonuniform, and the statistical results also indicated that the particle size distribution was quite broad (Figure S1). From the TEM results of Pt@NC–X catalysts, it was found that the Pt@NC–400 catalyst showed the narrowest particle size distribution, indicating that it had the most uniform dispersion of Pt. It can be speculated that this advantage might enable it to exhibit better stability.

The microscopic morphology of the Pt@NC–400 catalyst was observed via scanning electron microscopy (SEM), as shown in Figure 4. It can be observed that the material has a well-defined nanowire structure, which is embedded with many uniform metal nanoparticles on its surface. This structure is attributed to the fact that, during the preparation process, H₂PtCl₆ oxidized the aniline to PANI and, at the same time, was itself reduced to

platinum nanoparticles, which eventually led to the PANI-Pt precursor [29]. After high-temperature pyrolysis, its nanofiber structure remained intact, and platinum particles were still adequately dispersed on the support, as can be seen in Figure 4. It has been previously noted that the addition of a strong reducing agent, aniline, causes the rapid nucleation of nanocrystals and reduces the size of the Pt particles, thus maintaining a high degree of dispersion [29]. Furthermore, the nanofiber structure not only provides a large specific surface area and Pt active sites but also facilitates the diffusion of reactants and products, which further improves the catalytic activity of the reaction. While Figure S2 shows that the morphology of the 20% Pt/C catalyst presents an irregular bulk with messy stacking and a dense surface, it has a lower specific surface area and a poorer pore structure compared to the Pt@NC-400 catalyst (Table S2, Figure S3). It can be speculated that Pt@NC-400 may have a better performance in terms of diffusion processes, such as the adsorption and desorption of the substrate and product.

The elemental mapping of Pt@NC-400 was analyzed by dark-field scanning transmission electron microscopy (DF-STEM) and energy dispersive spectroscopy (EDS), as shown in Figure 5. The catalyst is mainly composed of the elements C, N, and Pt (Figure 5b–e), and their relative atomic ratios are 61.0, 9.2, and 29.8% (Table S3), respectively. The Pt metal particles are adequately dispersed, as shown in Figure 5a,f. Moreover, C and N are homogeneously dispersed in the support substrate, in which the metal Pt catalytic sites are uniformly embedded.

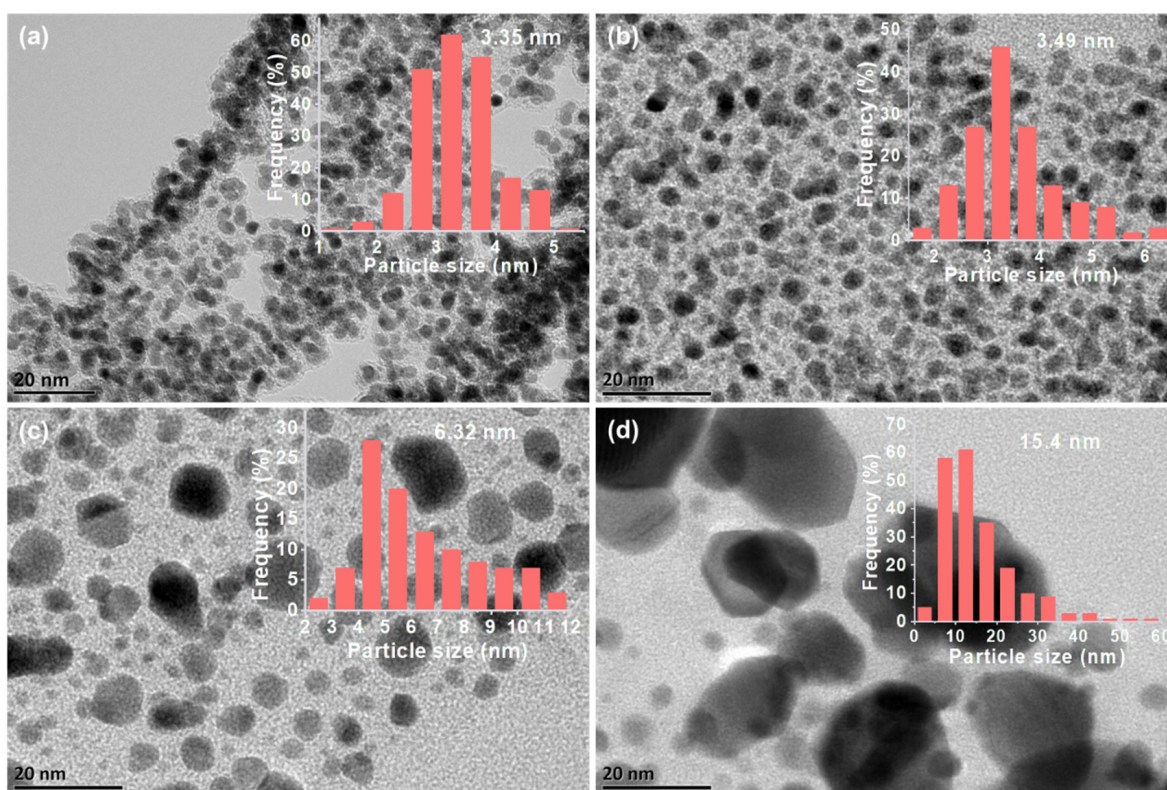


Figure 3. TEM images and particle size distributions of Pt-based catalysts obtained after the pyrolysis of PANI-Pt precursors at (a) 400 °C, (b) 500 °C, (c) 600 °C, and (d) 700 °C, respectively.

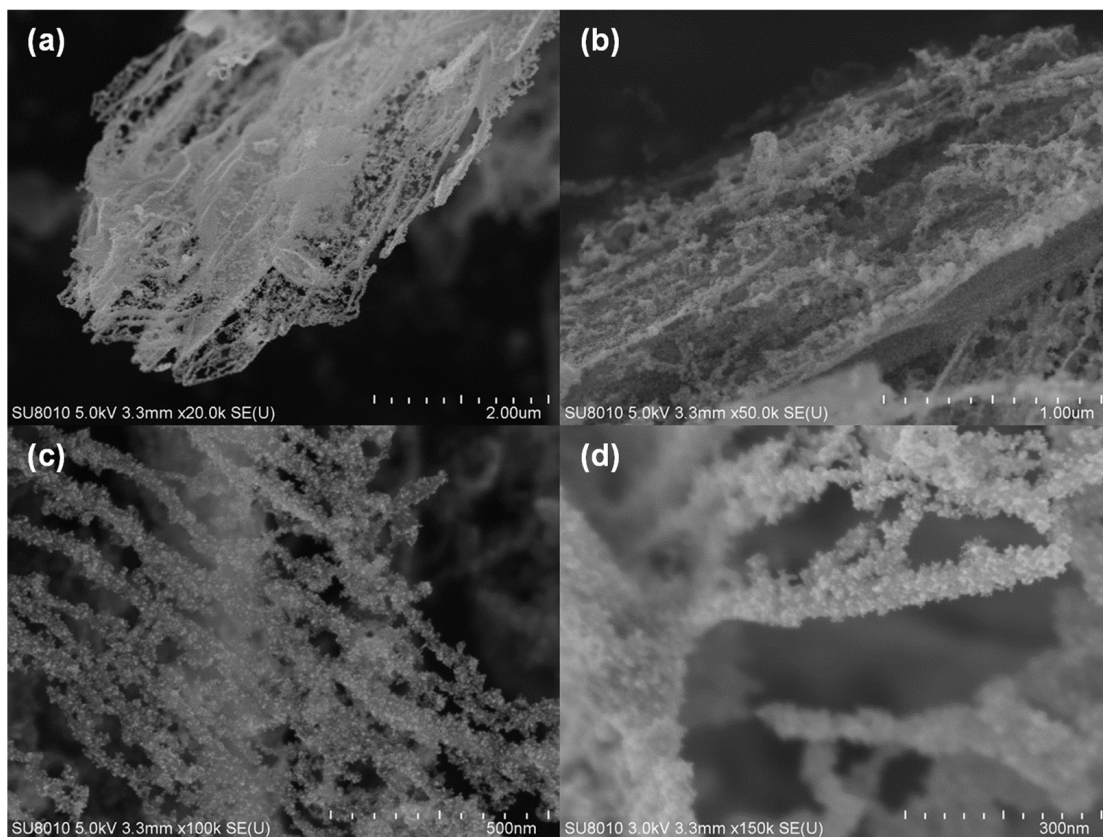


Figure 4. Representative SEM images of the Pt@NC-400 catalyst. (a–d) show the localized morphology of the catalyst with increasing magnification.

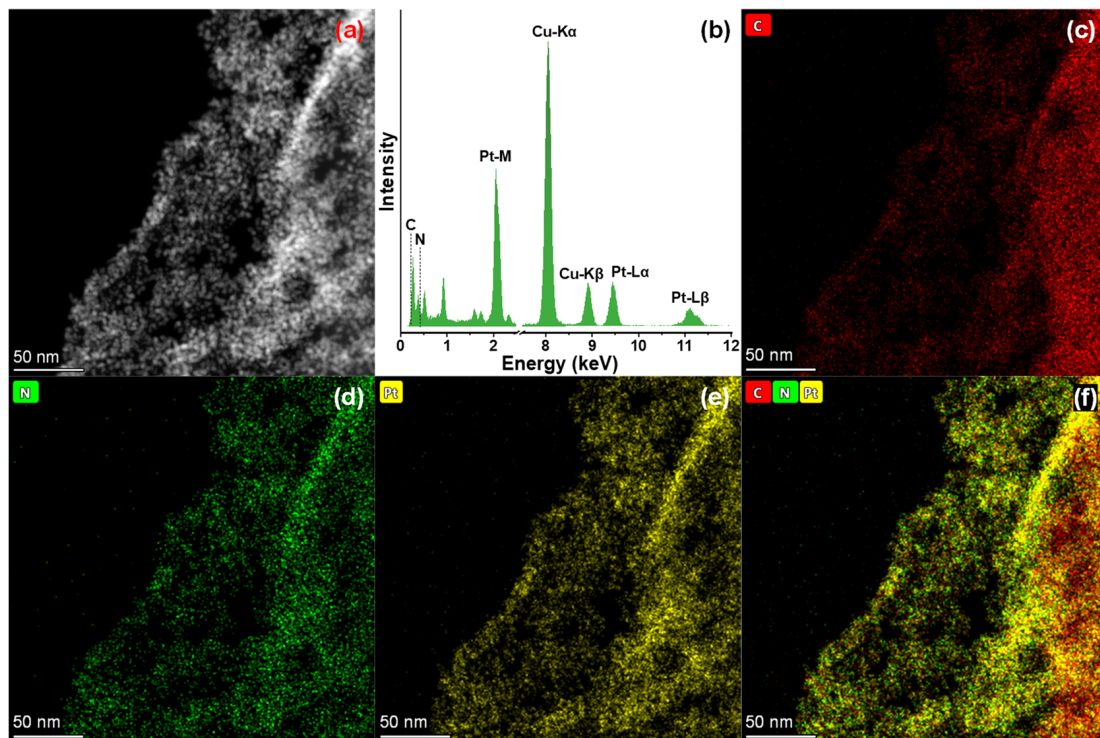


Figure 5. (a) DF-STEM image, (b) EDS elemental spectrum, (c–f) EDS elemental mapping of C, N, Pt, and the combination of C/N/Pt elements of the Pt@NC-400 catalyst.

2.1.3. Electronic Properties of the Pt@NC-400 Catalyst

The chemical valence states of the elements were subsequently investigated using XPS on the surface of the Pt@NC-400 catalyst (Figure 6). The surveyed spectra show that the material consists of Pt, C, N, and O (Figure 6a), which is in agreement with the EDS results. The C 1s spectrum (Figure 6b) can be resolved into three peaks corresponding to C-C (284.8 eV), C-N/C-O (286.3 eV), and O-C=O (288.7 eV). Three different chemical states of nitrogen could exist on the catalyst surface (Figure 6c), and the characteristic peaks at 399.2 eV, 400.4 eV, and 402.1 eV correspond to the Pt-N bond of quinone imine (=N-), the amino-nitrogen bond of aniline compounds (-NH-), and the polarizable sub-species (-NH⁺-) of nitrogen, respectively [29]. Both of these two spectra reveal the successful doping of nitrogen in the carbon support. The narrow scanning Pt 4f XPS spectrum of Pt@NC-400 (Figure 6d) shows the presence of two different valence states of Pt species on the catalyst surface, and the characteristic peaks are attributed to Pt⁰ (71.3 eV) and Pt⁴⁺ (72.8 eV), with percentages of 98.8 and 1.2, respectively (Table S4).

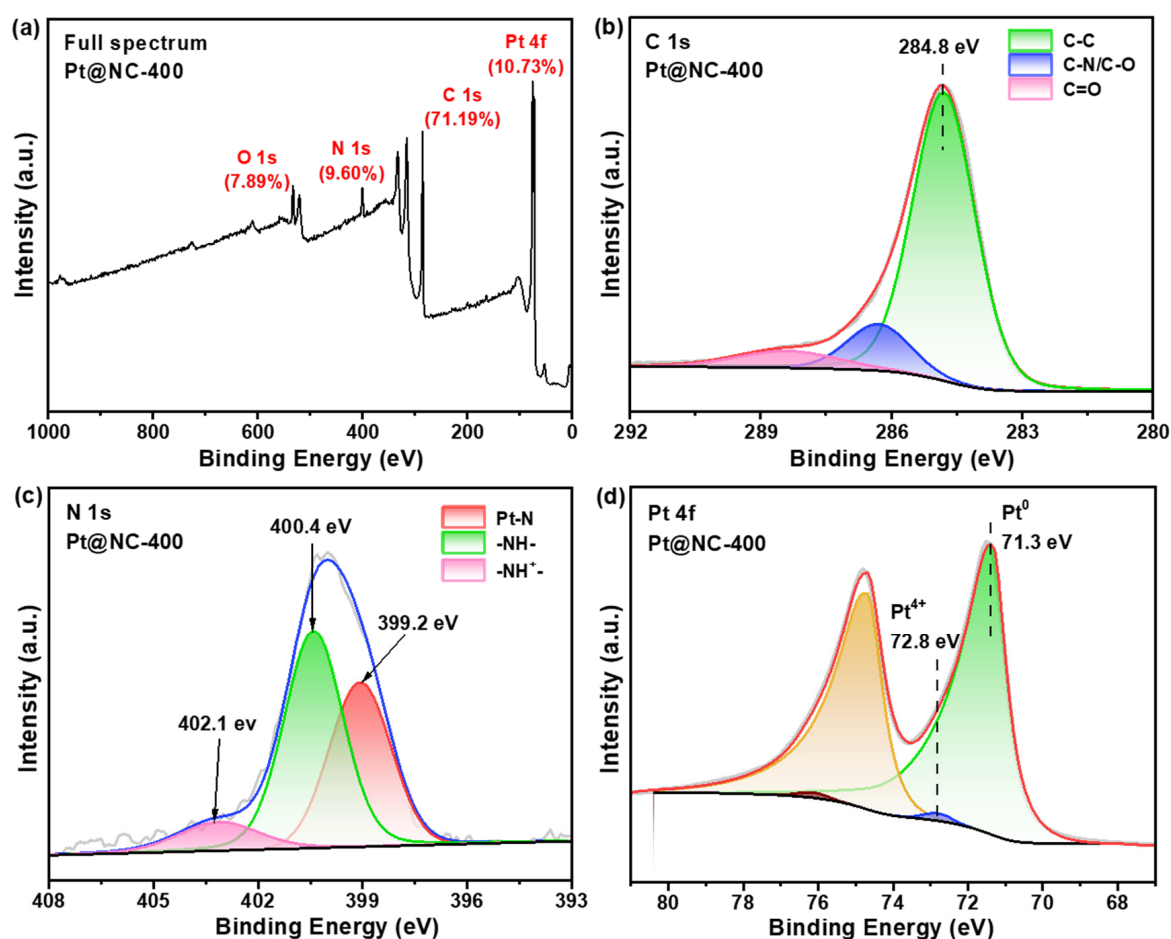


Figure 6. XPS spectra (a) Full spectrum, (b) C 1s, (c) N 1s, and (d) Pt 4f of the reduced Pt@NC-400 catalyst.

2.1.4. Chemical Structure of Functional Groups within Two Catalysts

Possible functional groups in the support of the Pt@NC-400 and 20% Pt/C catalysts were analyzed using FT-IR spectra, and their results are shown in Figure 7. It can be found that there are abundant characteristic absorption peaks in the infrared spectrum of the Pt@NC-400 catalyst, indicating its complicated structure. The absorption peak at 3431 cm⁻¹ was contributed to via the stretching vibration of -NH- linked to the benzenoid ring in the PANI, and the peak at 746 cm⁻¹ probably represents its out-of-plane rocking vibration. And the 1613 cm⁻¹ peak can be attributed to the stretching vibration of the C=C bond in the structure of the N=Q=N (Q stands for the quinone ring). The peak at

1450 cm^{-1} is the stretching vibration of the C=C bond in the benzene ring skeleton, while the peak at 1324 cm^{-1} indicates the stretching vibration of the C–N bond in the secondary aromatic amine. Also, the peak at 1236 cm^{-1} is associated with the deprotonated C–N group, and the absorption peak at 1114 cm^{-1} is ascribed to the in-plane bending mode of the aromatic C–H. All these characteristic peaks correspond to the characteristic bands of the PANI–Pt bond in the Pt@NC–400 catalyst [29,31], which provides evidence for the oxidation of aniline via H_2PtCl_6 to PANI and Pt particles. By contrast, the absorption peaks in the IR spectrum of the 20% Pt/C catalyst are fewer, and the absorption peaks at 3382, 1586, and 1265 cm^{-1} can be attributed to adsorbed water, the stretching vibration of C=C, and stretching vibration of C–O/C, respectively. On the other hand, the peaks at 553 and 559 cm^{-1} could be attributed to the in-plane bending vibrations of the C–O bond.

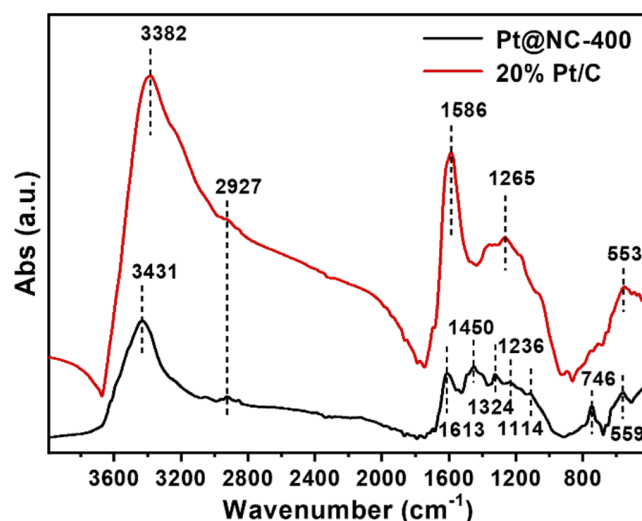


Figure 7. FT–IR spectra of Pt@NC–400 and 20% Pt/C catalysts.

2.2. APR Performance and Stability Testing of Different Catalysts

2.2.1. Influence of Pyrolysis Temperature on the Catalytic Activity of Pt@NC

It is well known that the size of active metal particles in nano-catalysts greatly affects their catalytic activity. Generally, the larger the particles of the active metal, the lower its surface free energy and the poorer the catalytic performance for a specific reaction. The preparation temperature here is an essential factor in controlling the size of Pt particles, so it is necessary to synthesize catalysts at different pyrolysis temperatures to investigate the APRM performance.

Figure 8a presents a comparison of the APRM performance of Pt-based catalysts after pyrolysis at different temperatures, and detailed data are listed in Table S5. It can be observed that the catalytic activity of the Pt@NC–400 is significantly higher than that of the rest catalysts, and its hydrogen production rate is 1013.4 $\mu\text{mol}_{\text{H}_2}/\text{g}_{\text{cat.}}/\text{s}$, which is about 2.5–5 times higher than other cases. Unexpectedly, the activity of Pt@NC pyrolyzed at 300 $^{\circ}\text{C}$ and is also low (391.6 $\mu\text{mol}_{\text{H}_2}/\text{g}_{\text{cat.}}/\text{s}$) compared to Pt@NC–400, although its particle size is smaller. This may be due to the insufficient decomposition of polyaniline in the support, resulting in the limited exposure of Pt active sites and finally leading to the poor catalytic activity of the Pt@NC–300 catalyst. When the temperature is over 400 $^{\circ}\text{C}$, the Pt particles in the Pt@NC–X catalysts grow rapidly, from 3.5 to 15.4 nm, as the pyrolysis temperature increases, which leads to a decrease in Pt dispersion and active sites, thus resulting in a reduction in the catalytic activity of the catalyst and a drop in the hydrogen production rate from 363.5 to 186.0 $\mu\text{mol}_{\text{H}_2}/\text{g}_{\text{cat.}}/\text{s}$. It can also be observed that Pt@NC–400 exhibits the highest ATOF as well, i.e., 4242 h^{-1} , which is 2.6–5.5 times higher than that of the other catalysts. This is most possibly related to the size of the Pt particles and the amount of active Pt in the catalyst.

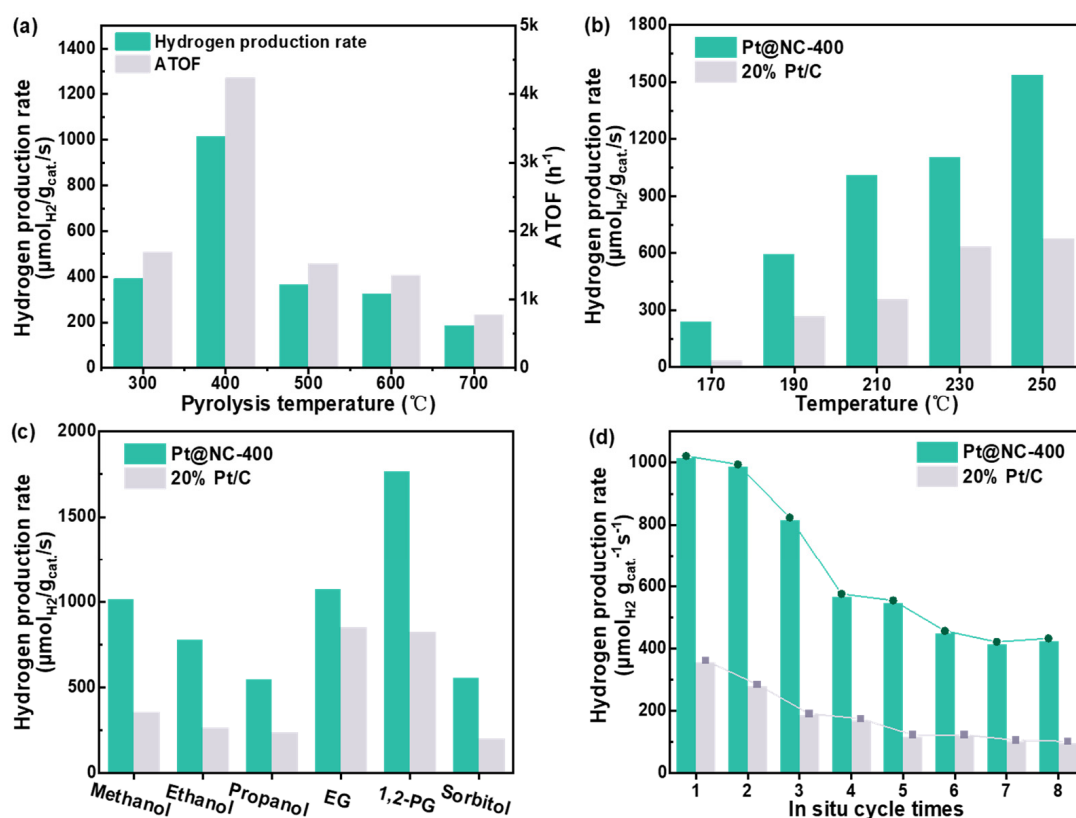


Figure 8. APR performance tests. (a) APRM performance of Pt@NC–X, where X represents the different pyrolysis temperatures, i.e., 300, 400, 500, 600, and 700 °C. (b) APRM performance of Pt@NC–400 and 20% Pt/C under different reaction temperatures. (c) APRM performance of Pt@NC–400 and 20% Pt/C with different substrates; the molar ratios of methanol, ethanol, propanol, ethylene glycol (EG), 1,2-propanol (1,2-PG), and sorbitol to water are 1:3, 1:3, 1:5, 1:2, 1:4, and 1:6, respectively. And (d) APRM stability tests for Pt@NC–400 and 20% Pt/C. The reaction conditions were as follows: all tests in (a–d) used 2 mg of catalyst, 5 mL of aqueous alcohol solution, 1.25 h reaction time, and a reaction temperature of 210 °C (except for (b)).

Five replicate experiments on the APRM activity of Pt@NC–400 catalysts were carried out at 210 °C using exactly the same reaction conditions, and the results were statistically analyzed, as shown in Table S6. It was found that the hydrogen production rates of the five experiments were very close to each other, with an average value of $974.2 \mu\text{mol}_{\text{H}_2}/\text{g}_{\text{cat.}}/\text{s}$ and a relative average deviation of only 2.66%, which indicates that the reproducibility of the experiments was very high.

2.2.2. APRM Catalytic Activity of the Pt@NC–400 and 20% Pt/C Catalysts

The APRM activity of Pt@NC–400 and commercial 20% Pt/C catalysts was also tested under different reaction temperatures. From the experimental results in Figure 8b and Table S7, it can be seen that, in general, the hydrogen production performance of both Pt@NC–400 and 20% Pt/C catalysts improved significantly with a temperature increase in the range of 170–250 °C, from 240.1 to $1536.6 \mu\text{mol}_{\text{H}_2}/\text{g}_{\text{cat.}}/\text{s}$ for Pt@NC–400 and from $34.8 \mu\text{mol}_{\text{H}_2}/\text{g}_{\text{cat.}}/\text{s}$ to $676.5 \mu\text{mol}_{\text{H}_2}/\text{g}_{\text{cat.}}/\text{s}$ for 20% Pt/C, respectively. It can be noted that the rate of Pt@NC–400 was always higher than that in 20% Pt/C under the same reaction temperature. In addition, the ATOF of both catalysts also saw a remarkable increase from 1256.2 to 6462.4 h^{-1} and 266.4 to 5177.8 h^{-1} for Pt@NC–400 and 20% Pt/C, respectively. It is believed that these results are quite likely attributed to the combination of higher Pt loading, a more active Pt metal surface area (Table S2, Figure S3), and a smaller particle size of Pt@NC–400 than 20% Pt/C. On the contrary, the selectivity of CO showed a negative trend with the increase in temperature (from 10.99 to 0.62% for

Pt@NC-400 and 40.16 to 0.30% for 20% Pt/C, respectively; see detailed data in Table S7), indicating an increased activity of the WGS reaction in both catalysts. The hydrogen production rate of Pt@NC-400 at 210 °C is 1013.4 $\mu\text{mol}_{\text{H}_2}/\text{g}_{\text{cat.}}/\text{s}$, which is 2.8 times higher than that of 20% Pt/C (357.3 $\mu\text{mol}_{\text{H}_2}/\text{g}_{\text{cat.}}/\text{s}$). The ATOFs of these two catalysts at 210 °C are 4242.1 h^{-1} (Pt@NC-400) and 2734.9 h^{-1} (20% Pt/C), respectively, with the former being 1.6 times higher than that of the latter, which is less than the ratio between their hydrogen production rates. This may be attributed to the different loading of Pt and/or the corresponding number of active sites in these two catalysts. While their CO selectivity at this 210 °C is still relatively high, i.e., 3.20% (Pt@NC-400) and 2.92% (20% Pt/C), respectively, only when the temperature reaches 230 °C does the selectivity drop to less than 1% (Table S7).

2.2.3. Evaluation of APR Performance of Different Feedstocks

In addition, we also tested the APR hydrogen production performance of Pt@NC-400 and 20% Pt/C catalysts using different small-molecule alcohol solutions, and the results are shown in Figure 8c and Table S8. It reveals that both the hydrogen production rate and ATOF of Pt@NC-400 are higher than those of 20% Pt/C in the APR reaction with various methanol substitution solutions (ethanol, propanol, ethylene glycol, 1,2 propanediol, and sorbitol), indicating that Pt@NC-400 has better catalytic activity. In addition, the CO selectivity in each non-methanol solution was found to be lower than that in methanol solutions. Furthermore, CO selectivity on Pt@NC-400 was generally lower than that on 20% Pt/C. It is worth noting that the 1,2-propylene glycol solution can raise the hydrogen production rate of Pt@NC-400 to 1766.5 $\mu\text{mol}_{\text{H}_2}/\text{g}_{\text{cat.}}/\text{s}$, which is much higher than with the methanol solution (1013.4 $\mu\text{mol}_{\text{H}_2}/\text{g}_{\text{cat.}}/\text{s}$, Table S6), and the CO selectivity is even lower with only 0.31% detected. All the results suggest that the Pt@NC-400 catalyst is more suitable and promising for catalyzing the APR hydrogen production reaction using small-molecule polyols and for the application of biomass to hydrogen conversion [23,34–38].

The hydrogen production performance of Pt-based catalysts, which catalyzed APR reactions in the recent literature, are summarized, as shown in Table S9. It was found that the catalytic performance of the Pt@NC-400 catalyst reached first-class overall. For example, under the same reaction conditions, the hydrogen production rate of the Pt@NC-400 catalyst was nearly 4.6 times that of the 2% Pt/ α -MoC [7] catalyst, but its ATOF was only 0.6 times that of the latter. This indicates that the present catalyst has higher mass-specific activity and lower intrinsic activity, which may be attributed to its higher Pt loading, more active metal sites, and larger particle size.

2.2.4. APRM Reaction Stability Test

Stability has always been a very important consideration for the development of a catalyst. Therefore, the catalytic stability of Pt@NC-400 and 20% Pt/C catalysts was finally investigated in a slurry bed reactor at a reaction temperature of 210 °C, as shown in Figure 8d. It can be seen that the hydrogen production rate of the Pt@NC-400 catalyst decreases rapidly in the third and fourth cycles, after which the activity declines slightly until the end of the eighth cycle, ending up at 423.9 $\mu\text{mol}_{\text{H}_2}/\text{g}_{\text{cat.}}/\text{s}$ and retaining 42% of its initial activity (1013.4 $\mu\text{mol}_{\text{H}_2}/\text{g}_{\text{cat.}}/\text{s}$), as presented in Table S10, which is still higher than the initial activity of the 20% Pt/C catalyst (356.9 $\mu\text{mol}_{\text{H}_2}/\text{g}_{\text{cat.}}/\text{s}$). The particle size of the spent Pt@NC-400 catalyst was analyzed using TEM. As shown in Figure S4a, the particle distribution of the spent Pt@NC-400 catalyst was still narrow, and the size changed little compared to the fresh catalyst after in situ cycling eight times, with an increase of only 1 nm to 4.35 nm. It is believed that the loss of the catalyst during cycling may be mainly responsible for its decrease in activity, and its actual stability may be better than that tested. While the activity of the 20% Pt/C catalyst also decreased throughout the testing, its hydrogen production rate after eight rounds was only 97.3 $\mu\text{mol}_{\text{H}_2}/\text{g}_{\text{cat.}}/\text{s}$, which is only 27% of its initial activity. The particle distribution of the spent 20% Pt/C catalyst broadened compared to the fresh catalyst (Figure S4b), and the size increased by 2 nm to

6.37 nm, which was much more significant. The above results indicate that Pt@NC-400 is also superior to the 20% Pt/C catalyst in terms of its stability.

3. Experimental Section

3.1. Materials

Methanol (GC, $\geq 99.9\%$), ethanol (GC, $>99.9\%$), propanol (GC, $\geq 99.9\%$), ethylene glycol (GC, $\geq 99.9\%$), 1,2-propylene glycol (GC, $\geq 99.5\%$), sorbitol (HPLC, $\geq 99.5\%$), and aniline (GC, $\geq 99.9\%$) were purchased from Shanghai Aladdin Biochemical Technology Co., Ltd. (Shanghai, China) $\text{H}_2\text{PtCl}_6 \cdot 6\text{H}_2\text{O}$ was purchased from Shaanxi Kaida Chemical Engineering Co., Ltd. (Baoji, China) Nitrogen (99.999%) and hydrogen (99.999%) were provided by Guangzhou Yuejia Gas Co., Ltd. (Guangzhou, China). All chemicals were used as-received without further purification. The water used in this work is ultrapure water, which was prepared in the laboratory with the Milli-Q Plus system.

3.2. Catalysts Preparation

Pt-based catalysts were prepared based on the reported method [29] with slight modifications, as presented in Figure 1. A typical synthesis procedure is as follows: 3.35 g of aniline was dissolved in 40 mL of ethanol, adding a certain amount of 5 wt.% H_2PtCl_6 to the aqueous solution, which was then aged overnight with stirring. All the above steps were performed at room temperature. Subsequently, the resulting slurry was vacuum-filtered, and the obtained purple precipitate was then washed with water until the filtrate became colorless. After drying the precipitate under a vacuum at $60\text{ }^\circ\text{C}$ for 12 h, the precursor PANI-Pt was obtained. Following this, PANI-Pt was pyrolyzed at $300\text{--}700\text{ }^\circ\text{C}$ for 2 h in flowing N_2 (50 mL min^{-1}) at a heating rate of $1\text{ }^\circ\text{C min}^{-1}$. After cooling down to room temperature, the N-doped Pt-based catalysts were obtained, which were named Pt@NC-X, where X represents the pyrolysis temperature.

3.3. Catalysts Characterizations

Powder X-ray diffraction (XRD) patterns were recorded using a Bruker D8 Advance diffractometer and $\text{Cu K}\alpha_1$ ($\lambda = 0.15406\text{ nm}$) radiation. The operation conditions were 40 kV and 30 mA with a scanning step of 0.01° and a rate of $10^\circ/\text{min}$ in the 2θ range of $5\text{--}80^\circ$. Crystalline phase identification was conducted by comparing the obtained XRD patterns with the PDF standard cards.

A Micromeritics ASAP 2020 sorption analyzer was used for the nitrogen adsorption and desorption measurements. Before measuring at $-196\text{ }^\circ\text{C}$, the samples were degassed at $350\text{ }^\circ\text{C}$ for 2 h. The specific surface area was calculated based on the Brunauer-Emmett-Teller (BET) equation.

The CO-pulse chemisorption experiment was performed on a Micromeritics Auto Chem II 2920 system to determine the specific area of exposed and active Pt^0 in reduced Pt-based catalysts. The samples were reduced in situ in flowing 10% H_2/Ar (50 mL/min) at $200\text{ }^\circ\text{C}$ for 2 h and then cooled to $50\text{ }^\circ\text{C}$ in flowing Ar. Afterward, CO chemisorption was performed via pulsing a mixture of 10% CO/Ar (50 mL/min). The number of surface Pt atoms was calculated based on a stoichiometric ratio of Pt to CO of 1.

Inductively coupled plasma optic emission spectrometry (ICP-OES) analysis was used to determine the Pt loading of the catalysts using an Agilent 720 spectrometer equipped with a VistaChip II catalytic combustion detector (CCD). A certain amount of this sample was dissolved in aqua regia and diluted to 50 mL of aqueous solution to test the metal content, which was expressed in wt.%.

Scanning electron microscope (SEM) images were obtained on a HITACHI SU8010 electron microscope operated at an accelerating voltage of 5 kV. Transmission electron microscope (TEM) images were taken on a Thermo Fisher Scientific Talos F200S electron microscope and operated at an accelerating voltage of 200 kV.

FT-IR spectra were examined by a Thermo Fisher Scientific Fourier infrared spectrometer with a scanning time of 32, a resolution of 4.000, a sampling gain of 1.0, a moving mirror speed of 0.4747, a diaphragm of 100.00, and a detector of DTGS KBr.

X-ray photoelectron spectroscopy (XPS) was carried out on a Thermo Fisher Scientific ESCALAB 250Xi spectrometer using a monochromatic Al K α source ($h\nu = 1486.6$ eV, $P = 150$ W) for excitation and a scanning beam spot with a diameter of 650 μm . The test results were calibrated with the C 1s signal (284.8 eV) as a reference.

3.4. Catalytic Activity Tests

3.4.1. Aqueous-Phase Reforming (APR) Reactions

APR reactions were conducted in a 30 mL stainless steel autoclave. The specific molar ratios of methanol, ethanol, propanol, ethylene glycol, 1,2-propanediol, and sorbitol to water were 1:3, 1:3, 1:5, 1:2, 1:4, and 1:6, respectively. Before the test, 2 mg Pt@NC-X or 20% Pt/C catalyst was activated with H_2 at 200 $^\circ\text{C}$ for 2 h under atmospheric pressure. The aqueous alcohol solution was injected into the reduction tubes to prevent the catalyst from contacting air, and then the reduced catalyst and reaction solution were introduced into the autoclave equipped with magnetic stirring. The reactor was then sealed, purged three times, and pressurized to 2.0 MPa with N_2 . Subsequently, all reactions were performed at 210 $^\circ\text{C}$ for 1.25 h, except for Section 2.2.2, where the reaction temperatures were 170, 190, 210, 230, and 250 $^\circ\text{C}$, respectively. Then, H_2 , CO, and CH_4 in the gaseous phase products were quantitatively analyzed using an Agilent 7980 gas chromatograph equipped with TCD and FID detectors and using a multipoint calibration method.

The APRM stability tests of the Pt@NC-400 and 20% Pt/C catalysts were performed using the same reactor, conditions, and analytical methods as their APRM performance tests. The in situ cycling reaction mode was adopted, where at the end of each round of the reaction, the supernatant in the batch reactor was replaced with the fresh reaction solution, and the spent catalyst was used for the next round. At the end of the eighth round, the spent catalysts were analyzed using TEM.

3.4.2. Catalyst Activity Evaluation Methods

The H_2 production rate ($\mu\text{mol}_{\text{H}_2}/\text{g}_{\text{cat.}}/\text{s}$) is used to describe the activity of the catalysts in catalyzing the APR reactions and is calculated as Equation (1) to ascertain how many μmol of hydrogen are produced per gram of the catalyst per second.

$$v_{\text{H}_2} = \frac{n_{\text{H}_2}}{t \times m_{\text{cat.}}} \quad (1)$$

where n_{H_2} is the mole of H_2 produced, $m_{\text{cat.}}$ is the mass of the catalyst used, t is the reaction time, and v_{H_2} is the hydrogen production rate.

The ATOF ($\text{mol}_{\text{H}_2}/\text{mol}_{\text{Pt}}/\text{h}$) is used to evaluate the average rate of hydrogen production per mole of Pt in the catalyst and is calculated based on Equation (2):

$$\text{ATOF} = \frac{n_{\text{H}_2}}{t \times n_{\text{Pt}}} \quad (2)$$

where n_{H_2} is the mole of H_2 produced, n_{Pt} is the mole of Pt in the catalyst used, and t is the reaction time.

The selectivity of CO is defined as the molar ratio of CO to all products in the gas phase and is calculated via Equation (3).

$$S_{\text{CO}} = \frac{n_{\text{CO}}}{n_{\text{H}_2} + n_{\text{CO}}} \times 100\% \quad (3)$$

$$n_i = x_i * \frac{V_{\text{total}}}{V_m} \quad (4)$$

where S_{CO} is the selectivity of CO, n_i is the moles of i ($i = H_2$ and CO), V_{total} is the total volume of the gas after the reaction, x_i is the mole fraction of each gaseous component, calculated by the external standard method, and V_m is the molar volume of the ideal gas at an ambient temperature. Alkanes were not detected by GC, and their content was not analyzed. Since CO₂ is highly soluble at high temperatures and pressure, and it is easily removed during the process of hydrogen purification, its content is not analyzed here either.

4. Conclusions

In conclusion, the above results obtained from the experiment and characterization show that a high-loaded and highly dispersed Pt@NC-400 catalyst with the desired APR performance and stability was successfully synthesized through a simple method. The Pt@NC-400 catalyst mainly consists of Pt, C, N, and O elements with uniformly dispersed Pt nanoparticles in the support matrix, and the particle size was only about 3 nm. During the formation of the PANI-Pt precursor, H₂PtCl₆ oxidizes aniline to PANI while being reduced to Pt particles, resulting in the nanofiber structure of the precursor. The presence of the strong reducing agent aniline causes the rapid nucleation of the nanocrystals and reduces the size of the Pt particles. And the strong integration of PANI and Pt nanoparticles keeps the nanofiber structure and the size of Pt particles basically unchanged during the pyrolysis process, thus maintaining the high dispersion of Pt.

Catalytic hydrogen production experiments with a methanol–water solution are conducted in a slurry bed reactor. The H₂ production rate obtained from Pt@NC-400 was 1013.4 μmol_{H₂}/g_{cat.}/s at 210 °C, which is much higher than that of 20% Pt/C (357.3 μmol_{H₂}/g_{cat.}/s). Besides methanol, the Pt@NC-400 catalyst performed with high efficiency in hydrogen production reactions of other liquid alcohols (ethanol, propanol, ethylene glycol, 1,2 propanediol, and sorbitol) and even reached a high hydrogen production rate of 1766.5 μmol_{H₂}/g_{cat.}/s in catalyzing 1,2-propanediol-water reforming. The stability of Pt@NC-400 is also much better than that of 20% Pt/C. These results may be attributed to the high loading of Pt as well as superior metal dispersion, more active sites, high intrinsic activity, and good structural stability of the Pt@NC-400 catalyst. It is believed that the catalytic properties of a catalyst are greatly influenced by its structure. As this catalyst preparation method is facile and reproducible, it can easily be scaled up for practical applications. This work illustrates a new strategy for preparing efficient and durable Pt-based catalysts for APR.

Supplementary Materials: The following supporting information can be downloaded at: <https://www.mdpi.com/article/10.3390/catal13111428/s1>, [7,18,39–44]; Figure S1. (a) TEM image of 20% Pt/C; (b) statistical distribution of Pt particle size of 20% Pt/C; Figure S2. SEM images of 20% Pt/C catalyst; Figure S3. N₂ adsorption and desorption curves and the CO pulse chemisorption curves of Pt@NC-400 and 20% Pt/C catalysts; Figure S4. TEM images and particle size distributions of the spent Pt@NC-400 (a) and 20% Pt/C (b) catalysts after 8 times of in-situ cycling reaction; Table S1. The particle size of Pt@NC-X catalysts; Table S2. Main physiochemical properties of Pt@NC-400 and 20% Pt/C catalysts; Table S3. Relative atomic ratios of the elements C, N, and Pt in the Pt@NC-400 catalyst measured by EDS; Table S4. Data statistics for the Pt 4f spectrum of Pt@NC-400 catalysts; Table S5. APRM performance of Pt-based catalysts at different pyrolysis temperatures; Table S6. Reproducibility test of APRM reaction catalyzed by Pt@NC-400; Table S7. APRM performance of Pt@NC-400 and 20% Pt/C catalysts at different reaction temperatures; Table S8. Differences in APR catalytic performance between Pt@NC-400 and 20% Pt/C catalysts under different feedstocks; Table S9. Hydrogen production performance of APR catalyzed by Pt-based catalysts in recent literature; Table S10. Catalytic stability performance of Pt@NC-400 and 20% Pt/C catalysts at 210 °C.

Author Contributions: Z.X.: Conceptualization, Methodology, Investigation, Validation, Visualization, and Writing—original draft. X.L.: Conceptualization, Methodology, Investigation, Validation, and Visualization. W.F. and B.C.: Conceptualization and Methodology. Q.M.: Conceptualization, Methodology, Writing—review and editing, Supervision, and Funding acquisition. T.W.: Methodology, Writing—review and editing, Resources, Supervision, and Funding acquisition. All authors have read and agreed to the published version of the manuscript.

Funding: This work was supported by the Basic Research and Applicable Basic Research in Guangzhou City (202201010429) and the Guangdong Provincial Key Laboratory of Plant Resources Biorefinery (2021GDKLPRB09).

Data Availability Statement: The data presented in this study are available on request from the corresponding author.

Acknowledgments: We are very grateful to Catalysts journal for funding our Article Processing Charge (APC).

Conflicts of Interest: The authors declare that they have no known competing financial interest or personal relationships that could have appeared to influence the work reported in this paper.

References

1. Barreto, L.; Makihira, A.; Riahi, K. The hydrogen economy in the 21st century: A sustainable development scenario. *Int. J. Hydrog. Energy* **2003**, *28*, 267–284. [[CrossRef](#)]
2. Olah, G.A. Towards Oil Independence through Renewable Methanol Chemistry. *Angew. Chem. Int. Ed.* **2013**, *52*, 104–107. [[CrossRef](#)] [[PubMed](#)]
3. Cook, T.R.; Dogutan, D.K.; Reece, S.Y.; Surendranath, Y.; Teets, T.S.; Nocera, D.G. Solar Energy Supply and Storage for the Legacy and Nonlegacy Worlds. *Chem. Rev.* **2010**, *110*, 6474–6502. [[CrossRef](#)] [[PubMed](#)]
4. Lewis, N.S. Powering the Planet. *MRS Bull.* **2011**, *32*, 808–820. [[CrossRef](#)]
5. Grätzel, M. Powering the planet. *Nature* **2000**, *403*, 363. [[CrossRef](#)]
6. Chen, L.-N.; Hou, K.-P.; Liu, Y.-S.; Qi, Z.-Y.; Zheng, Q.; Lu, Y.-H.; Chen, J.-Y.; Chen, J.-L.; Pao, C.-W.; Wang, S.-B.; et al. Efficient Hydrogen Production from Methanol Using a Single-Site Pt1/CeO2 Catalyst. *J. Am. Chem. Soc.* **2019**, *141*, 17995–17999. [[CrossRef](#)]
7. Lin, L.; Zhou, W.; Gao, R.; Yao, S.; Zhang, X.; Xu, W.; Zheng, S.; Jiang, Z.; Yu, Q.; Li, Y.W.; et al. Low-temperature hydrogen production from water and methanol using Pt/alpha-MoC catalysts. *Nature* **2017**, *544*, 80–83. [[CrossRef](#)]
8. Schlapbach, L.; Züttel, A. Hydrogen-storage materials for mobile applications. *Nature* **2001**, *414*, 353–358. [[CrossRef](#)] [[PubMed](#)]
9. Huang, Y.J.; Cheng, Y.H.; Zhang, J.Y. A Review of High Density Solid Hydrogen Storage Materials by Pyrolysis for Promising Mobile Applications. *Ind. Eng. Chem. Res.* **2021**, *60*, 2737–2771. [[CrossRef](#)]
10. Liu, Y.F.; Ren, Z.H.; Zhang, X.; Jian, N.; Yang, Y.X.; Gao, M.X.; Pan, H.G. Development of Catalyst-Enhanced Sodium Alanate as an Advanced Hydrogen-Storage Material for Mobile Applications. *Energy Technol.-Ger.* **2018**, *6*, 487–500. [[CrossRef](#)]
11. Wismann, S.T.; Engbaek, J.S.; Vendelbo, S.B.; Bendixen, F.B.; Eriksen, W.L.; Aasberg-Petersen, K.; Frandsen, C.; Chorkendorff, I.; Mortensen, P.M. Electrified methane reforming: A compact approach to greener industrial hydrogen production. *Science* **2019**, *364*, 756–759. [[CrossRef](#)]
12. Callison, J.; Subramanian, N.D.; Rogers, S.M.; Chutia, A.; Gianolio, D.; Catlow, C.R.A.; Wells, P.P.; Dimitratos, N. Directed aqueous-phase reforming of glycerol through tailored platinum nanoparticles. *Appl. Catal. B-Environ.* **2018**, *238*, 618–628. [[CrossRef](#)]
13. Debek, R.; Motak, M.; Galvez, M.E.; Grzybek, T.; Da Costa, P. Promotion effect of zirconia on Mg(Ni,Al)O mixed oxides derived from hydrothermal synthesis in CO2 methane reforming. *Appl. Catal. B-Environ.* **2018**, *223*, 36–46. [[CrossRef](#)]
14. Zou, X.X.; Zhang, Y. Noble metal-free hydrogen evolution catalysts for water splitting. *Chem. Soc. Rev.* **2015**, *44*, 5148–5180. [[CrossRef](#)] [[PubMed](#)]
15. Jiang, X.S.; Wen, X.H.; Xu, H.P. Study on isolated boost full bridge converter in FCEV. In Proceedings of the Ipec: 2005 International Power Engineering Conference, Singapore, 29 November–2 December 2005; Volumes 1 and 2, pp. 827–830. [[CrossRef](#)]
16. Pipitone, G.; Zoppi, G.; Pirone, R.; Bensaid, S. A critical review on catalyst design for aqueous phase reforming. *Int. J. Hydrog. Energy* **2022**, *47*, 151–180. [[CrossRef](#)]
17. Zoppi, G.; Pipitone, G.; Pirone, R.; Bensaid, S. Aqueous phase reforming process for the valorization of wastewater streams: Application to different industrial scenarios. *Catal. Today* **2022**, *387*, 224–236. [[CrossRef](#)]
18. Li, D.D.; Li, Y.; Liu, X.H.; Guo, Y.; Pao, C.W.; Chen, E.L.; Hu, Y.F.; Wang, Y.Q. NiAl₂O₄ Spinel Supported Pt Catalyst: High Performance and Origin in Aqueous-Phase Reforming of Methanol. *Acs Catal.* **2019**, *9*, 9671–9682. [[CrossRef](#)]
19. Kuhn, J.N.; Huang, W.; Tsung, C.-K.; Zhang, Y.; Somorjai, G.A. Structure Sensitivity of Carbon–Nitrogen Ring Opening: Impact of Platinum Particle Size from below 1 to 5 nm upon Pyrrole Hydrogenation Product Selectivity over Monodisperse Platinum Nanoparticles Loaded onto Mesoporous Silica. *J. Am. Chem. Soc.* **2008**, *130*, 14026–14027. [[CrossRef](#)] [[PubMed](#)]
20. Tsung, C.K.; Kuhn, J.N.; Huang, W.Y.; Aliaga, C.; Hung, L.I.; Somorjai, G.A.; Yang, P.D. Sub-10 nm Platinum Nanocrystals with Size and Shape Control: Catalytic Study for Ethylene and Pyrrole Hydrogenation. *J. Am. Chem. Soc.* **2009**, *131*, 5816–5822. [[CrossRef](#)] [[PubMed](#)]
21. Frelink, T.; Visscher, W.; van Veen, J.A.R. Particle size effect of carbon-supported platinum catalysts for the electrooxidation of methanol. *J. Electroanal. Chem.* **1995**, *382*, 65–72. [[CrossRef](#)]
22. Ravenelle, R.M.; Copeland, J.R.; Kim, W.-G.; Crittenden, J.C.; Sievers, C. Structural Changes of γ -Al₂O₃-Supported Catalysts in Hot Liquid Water. *Acs Catal.* **2011**, *1*, 552–561. [[CrossRef](#)]

23. Shabaker, J.W.; Davda, R.R.; Huber, G.W.; Cortright, R.D.; Dumesic, J.A. Aqueous-phase reforming of methanol and ethylene glycol over alumina-supported platinum catalysts. *J. Catal.* **2003**, *215*, 344–352. [[CrossRef](#)]
24. Kim, T.-W.; Kim, H.-D.; Jeong, K.-E.; Chae, H.-J.; Jeong, S.-Y.; Lee, C.-H.; Kim, C.-U. Catalytic production of hydrogen through aqueous-phase reforming over platinum/ordered mesoporous carbon catalysts. *Green Chem.* **2011**, *13*, 1718–1728. [[CrossRef](#)]
25. Vikla, A.K.K.; Simakova, I.; Demidova, Y.; Keim, E.G.; Calvo, L.; Gilarranz, M.A.; He, S.; Seshan, K. Tuning Pt characteristics on Pt/C catalyst for aqueous-phase reforming of biomass-derived oxygenates to bio-H₂. *Appl. Catal. A Gen.* **2021**, *610*, 117963. [[CrossRef](#)]
26. Lemus, J.; Bedia, J.; Calvo, L.; Simakova, I.L.; Murzin, D.Y.; Etzold, B.J.M.; Rodriguez, J.J.; Gilarranz, M.A. Improved synthesis and hydrothermal stability of Pt/C catalysts based on size-controlled nanoparticles. *Catal. Sci. Technol.* **2016**, *6*, 5196–5206. [[CrossRef](#)]
27. Liu, J. Catalysis by Supported Single Metal Atoms. *Acs Catal.* **2016**, *7*, 34–59. [[CrossRef](#)]
28. Zhang, S.; Liu, Y.; Zhang, M.; Ma, Y.; Hu, J.; Qu, Y. Sustainable production of hydrogen with high purity from methanol and water at low temperatures. *Nat. Commun.* **2022**, *13*, 5527. [[CrossRef](#)]
29. Liu, F.J.; Huang, L.M.; Wen, T.C.; Gopalan, A.; Hung, J.S. Interfacial synthesis of platinum loaded polyaniline nanowires in poly(styrene sulfonic acid). *Mater. Lett.* **2007**, *61*, 4400–4405. [[CrossRef](#)]
30. Cho, W.; Park, S.-J.; Kim, S. Effect of monomer concentration on interfacial synthesis of platinum loaded polyaniline nanocomplex using poly(styrene sulfonic acid). *Synth. Met.* **2011**, *161*, 2446–2450. [[CrossRef](#)]
31. Chen, Y.; Li, L.; Zhang, L.; Han, J. In situ formation of ultrafine Pt nanoparticles on surfaces of polyaniline nanofibers as efficient heterogeneous catalysts for the hydrogenation reduction of nitrobenzene. *Colloid Polym. Sci.* **2018**, *296*, 567–574. [[CrossRef](#)]
32. Xiong, Y.J.; Ma, Y.A.; Zou, L.L.; Han, S.B.; Chen, H.; Wang, S.; Gu, M.; Shen, Y.; Zhang, L.P.; Xia, Z.H.; et al. N-doping induced tensile-strained Pt nanoparticles ensuring an excellent durability of the oxygen reduction reaction. *J. Catal.* **2020**, *382*, 247–255. [[CrossRef](#)]
33. Liu, M.Y.; Hu, A.P.; Ma, Y.N.; Wang, G.L.; Zou, L.L.; Chen, X.H.; Yang, H. Nitrogen-doped Pt₃Co intermetallic compound nanoparticles: A durable oxygen reduction electrocatalyst. *J. Electroanal. Chem.* **2020**, *871*, 114267. [[CrossRef](#)]
34. Chang, A.C.C.; Louh, R.F.; Wong, D.; Tseng, J.; Lee, Y.S. Hydrogen production by aqueous-phase biomass reforming over carbon textile supported Pt–Ru bimetallic catalysts. *Int. J. Hydrog. Energy* **2011**, *36*, 8794–8799. [[CrossRef](#)]
35. Meryemoglu, B.; Hesenov, A.; Irmak, S.; Atanur, O.M.; Erbatur, O. Aqueous-phase reforming of biomass using various types of supported precious metal and raney-nickel catalysts for hydrogen production. *Int. J. Hydrog. Energy* **2010**, *35*, 12580–12587. [[CrossRef](#)]
36. Davda, R.R.; Dumesic, J.A. Renewable hydrogen by aqueous-phase reforming of glucose. *Chem. Commun.* **2004**, 36–37. [[CrossRef](#)]
37. Shabaker, J.W.; Huber, G.W.; Davda, R.R.; Cortright, R.D.; Dumesic, J.A. Aqueous-phase reforming of ethylene glycol over supported platinum catalysts. *Catal. Lett.* **2003**, *88*, 1–8. [[CrossRef](#)]
38. Huber, G.W.; Shabaker, J.W.; Dumesic, J.A. Raney Ni–Sn Catalyst for H₂ Production from Biomass-Derived Hydrocarbons. *Science* **2003**, *300*, 2075–2077. [[CrossRef](#)]
39. Lin, L.; Yu, Q.; Peng, M.; Li, A.; Yao, S.; Tian, S.; Liu, X.; Li, A.; Jiang, Z.; Gao, R.; et al. Atomically Dispersed Ni/alpha-MoC Catalyst for Hydrogen Production from Methanol/Water. *J. Am. Chem. Soc.* **2021**, *143*, 309–317. [[CrossRef](#)]
40. Davda, R.R.; Shabaker, J.W.; Huber, G.W.; Cortright, R.D.; Dumesic, J.A. Aqueous-phase reforming of ethylene glycol on silica-supported metal catalysts. *Appl. Catal. B Environ.* **2003**, *43*, 13–26. [[CrossRef](#)]
41. Larimi, A.; Khorasheh, F. Renewable hydrogen production over Pt/Al₂O₃ nano-catalysts: Effect of M-promoting (M=Pd, Rh, Re, Ru, Ir, Cr). *Int. J. Hydrog. Energy* **2019**, *44*, 8243–8251. [[CrossRef](#)]
42. Mao, Q.; Guo, Y.; Liu, X.; Shakouri, M.; Hu, Y.; Wang, Y. Identifying the realistic catalyst for aqueous phase reforming of methanol over Pt supported by lanthanum nickel perovskite catalyst. *Appl. Catal. B Environ.* **2022**, *313*, 121435. [[CrossRef](#)]
43. Lei, Y.; Lee, S.; Low, K.-B.; Marshall, C.L.; Elam, J.W. Combining Electronic and Geometric Effects of ZnO-Promoted Pt Nanocatalysts for Aqueous Phase Reforming of 1-Propanol. *Acs Catal.* **2016**, *6*, 3457–3460. [[CrossRef](#)]
44. Bossola, F.; Pereira-Hernández, X.I.; Evangelisti, C.; Wang, Y.; Dal Santo, V. Investigation of the promoting effect of Mn on a Pt/C catalyst for the steam and aqueous phase reforming of glycerol. *J. Catal.* **2017**, *349*, 75–83. [[CrossRef](#)]

Disclaimer/Publisher’s Note: The statements, opinions and data contained in all publications are solely those of the individual author(s) and contributor(s) and not of MDPI and/or the editor(s). MDPI and/or the editor(s) disclaim responsibility for any injury to people or property resulting from any ideas, methods, instructions or products referred to in the content.